Title

Automated body composition estimation from device-agnostic 3D optical scans in pediatric populations.

Journal

Clinical Nutrition, 42(9)

Authors

Tian, Isaac
Wong, Michael
Nguyen, William
et al.

Publication Date

2023-09-01

DOI

10.1016/j.clnu.2023.07.012

Peer reviewed

HHS Public Access

Author manuscript

Clin Nutr. Author manuscript; available in PMC 2024 September 01.

Published in final edited form as:

Clin Nutr. 2023 September ; 42(9): 1619–1630. doi:10.1016/j.clnu.2023.07.012.

Automated body composition estimation from device-agnostic 3D optical scans in pediatric populations

Isaac Y. Tian[*,1], **Michael C. Wong**[2], **William M. Nguyen**[1], **Samantha Kennedy**[3], **Cassidy McCarthy**[3], **Nisa N. Kelly**[2], **Yong E. Liu**[2], **Andrea K. Garber**[4], **Steven B. Heymsfield**[3], **Brian Curless**[1], **John A. Shepherd**[2]

[1]Paul G. Allen School of Computer Science and Engineering, University of Washington; Seattle, WA, 98195, USA.

[2]University of Hawaii Cancer Center, University of Hawaii - Manoa; Honolulu, HI, 96813, USA.

[3]Pennington Biomedical Research Center, Louisiana State University; Baton Rouge, LA, 70808, USA.

[4]UCSF School of Medicine, University of California - San Francisco, San Francisco, CA, 94118, USA

Abstract

Background: Excess adiposity in children is strongly correlated with obesity-related metabolic disease in adulthood, including diabetes, cardiovascular disease, and 13 types of cancer. Despite the many long-term health risks of childhood obesity, body mass index (BMI) Z-score is typically the only adiposity marker used in pediatric studies and clinical applications. The effects of regional adiposity are not captured in a single scalar measurement, and their effects on short- and long-term metabolic health are largely unknown. However, clinicians and researchers rarely deploy gold-standard methods for measuring compartmental fat such as magnetic resonance imaging (MRI) and dual X-ray absorptiometry (DXA) on children and adolescents due to cost or radiation concerns. Three-dimensional optical (3DO) scans are relatively inexpensive to obtain and use non-invasive and radiation-free imaging techniques to capture the external surface geometry of a patient's body. This 3D shape contains cues about the body composition that can be learned from

[*]Corresponding author. Phone #: 858-729- 8538; iytian@cs.washington.edu; Mailing: Paul G. Allen School of Computer Science & Engineering, University of Washington, Box 352355, Seattle, WA 98195-2355.

Author Contributions:

Isaac Y. Tian: Methodology, Software, Formal Analysis, Investigation, Writing – Original
Michael C. Wong: Methodology, Investigation, Writing – R&E
William M. Nguyen: Validation, Data Curation, Writing – R&E
Samantha Kennedy: Investigation, Writing – R&E
Cassidy McCarthy: Investigation, Writing – R&E
Nisa N. Kelly: Investigation, Writing – R&E, Data Curation, Project administration
Yong E. Liu: Investigation, Writing – R&E, Data Curation
Andrea K. Garber: Investigation, Writing – R&E, Funding Acquisition
Steven B. Heymsfield: Conceptualization, Methodology, Resources, Supervision, Funding Acquisition, Writing – R&E
Brian Curless: Conceptualization, Methodology, Resources, Supervision, Funding Acquisition, Writing – R&E
John A. Shepherd: Conceptualization, Methodology, Resources, Supervision, Funding Acquisition, Writing – R&E

a structured correlation between 3D body shape parameters and reference DXA scans obtained on a sample population.

Study Aim: This study seeks to introduce a radiation-free, automated 3D optical imaging solution for monitoring body shape and composition in children aged 5–17.

Methods: We introduce an automated, linear learning method to predict total and regional body composition of children aged 5–17 from 3DO scans. We collected 145 male and 206 female 3DO scans on children between the ages of 5 and 17 with three scanners from independent manufacturers. We used an automated shape templating method first introduced on an adult population to fit a topologically consistent 60,000 vertex (60k) mesh to 3DO scans of arbitrary scanning source and mesh topology. We constructed a parameterized body shape space using principal component analysis (PCA) and estimated a regression matrix between the shape parameters and their associated DXA measurements. We automatically fit scans of 30 male and 38 female participants from a held-out test set and predicted 12 body composition measurements.

Results: The coefficient of determination (R^2) between 3DO predicted body composition and DXA measurements was at least 0.85 for all measurements with the exception of visceral fat on 3D scan predictions. Precision error was 1–4 times larger than that of DXA. No predicted variable was significantly different from DXA measurement except for male trunk lean mass.

Conclusion: Optical imaging can quickly, safely, and inexpensively estimate regional body composition in children aged 5–17. Frequent repeat measurements can be taken to chart changes in body adiposity over time without risk of radiation overexposure.

Keywords

3D Scanning; Body Composition; Machine Learning; Pediatric obesity

INTRODUCTION

Obesity in childhood and adolescents strongly predicts lifelong obesity. More than half of obese children develop into obese adolescents, and around 70% of obese adolescents remain obese past age 30 [1]. Over the last 30 years, obesity has more than doubled in children under age 12, quadrupled in adolescents, and is linked to cardiovascular disease, insulin resistance, and 13 different types of cancer [2–6]. Body mass index (BMI) and its z-score (BMI-Z) are often used as analogues for adiposity but fail to capture both total and regional compositional differences between fat and lean mass, both of which are correlated with cardiometabolic risk. [7]

Despite the connections between pediatric obesity and lifelong metabolic disease risk, study of body composition analysis in pediatrics is limited. Gold standard imaging techniques to measure total and regional adiposity such as dual X-ray absorptiometry (DXA) requires exposure to ionizing radiation, which are potentially more harmful in children and adolescents and is used sparingly. MRI, although radiation free, is expensive to capture and unsustainable in both time and cost for frequent repeat monitoring. Children with behavioral conditions may be ineligible for both DXA and MRI due to compliance limitations at this

age bracket [8]. This is particularly problematic in pediatric research as people experience the largest rates of change in body mass and composition between the ages of 5 and 18 [9].

Intermediate alternatives to radiological imaging for adiposity measurement, such as bioelectric impedance, offer more information than BMI alone but have limited resolution in regional adiposity measurement. These methods extrapolate adiposity from scalar signals instead of directly imaging the body compartments contributing to total and regional adiposity [10, 11]. A non-radiological method that can accurately estimate the metrics measured by reference methods such as DXA without exposure to ionizing radiation could dramatically increase the survey frequency for metabolically at-risk children and adolescents during their critical developmental period of maximum compositional fluctuations.

3D optical (3DO) scanning is a radiation-free method of capturing external body shape using structured light (SL) or time of flight (ToF) imaging that is faster, safer, and relatively inexpensive compared to radiology. [12] 3DO scanning produces a 3D image of the surface geometry of a human body represented as a point cloud connected by edges in a graph structure. These 3D surfaces represented as unions of discrete points and their 3D spatial graph connections are defined as 3D meshes. Previous work on an adult cohort demonstrated that 3DO captured body shape is a strong signal for many of the body composition metrics measured by DXA. [13, 14] Additional studies on children aged 5–17 indicated similar correlations between 3D shape and body composition for a pediatric population [15]. A 3DO model for predicting body composition from scans for children would allow for safe and repeatable measurements of total and regional adiposity. As was the case in adults, this step was missing due to a lack of paired 3D to DXA data and the lack of standardized formats and interpretations for unstructured 3D mesh data. [16]

The purpose of our investigation was to develop a unified, input device-agnostic 3DO body composition prediction model for a pediatric population spanning the age range of 5–17. Our method standardizes randomly ordered point clouds captured by 3DO scanners into a common topology and builds a principal component parameterized shape space from the standardized mesh set. We derived predictions to DXA metrics from this shape space and tested its predictive capacity on held out 3DO scans. This method could be used for body composition monitoring in juvenile and adolescent patients without exposing them to potentially harmful radiation doses while also increasing the survey frequency for data acquisition, enabling longitudinal monitoring over shorter intervals. We hypothesized that our method would generate body composition predictions with accuracy and precision comparable to DXA, thus allowing for greater freedom and resolution in longitudinal studies of body composition for children and adolescents.

METHODS

This work builds upon the methods of [16] and is a cross-sectional study of a highly stratified sample of children that estimates body composition from unstructured 3DO scans and benchmarks accuracy against whole body DXA measures. We present an automated, device agnostic pipeline for converting raw, unorganized 3D optical scans into watertight and topologically consistent 60,001 vertex (60k) fitted mesh templates. From a set of

templated meshes produced by our method, we construct a parameterized 3D shape space using PCA and demonstrate its capacity to predict body composition measures with accuracies measured against DXA. The subset of DXA variables predicted in this study are fat mass, fat-free mass, percent fat, visceral fat, arm fat, leg fat, trunk fat, arm lean, leg lean, trunk lean, fat mass index, and fat-free mass index. In addition, we inverted the prediction equations to visualize how increments in certain body variables affect the 3D shape of a scanned subject, potentially providing clinicians a visualization tool for estimating longitudinal differences in a pediatric population whose bodies change much more rapidly in short time scales than an adult cohort.

We used the methods from [16] to standardize 145 male and 206 female scans from three different 3DO scanners to construct statistical models of body shape using principal component analysis (PCA). We computed linear regressions between the shape parameters of the PCA model and paired DXA composition measurements for all participants in the training set. We tested the predictive accuracy of our model on 132 held out 3DO scans (52 males). We used our shape model to extrapolate the body shape and composition of a younger child to an older age to visualize both the effects of intervention and aging versus no intervention.

Experimental Cohort

Our method was trained and tested on children and adolescents from the Shape Up! Kids Study (NIH R01 DK111698) and were recruited in the Honolulu, HI area at the University of Hawaii Cancer Center (UH), in the San Francisco, CA area at the University of California, San Francisco (UCSF), and in the Baton Rouge, LA area at Pennington Biomedical Research Center (PBRC). This work represents an intermediate analysis of an in-progress data collection project.

This was a cross-sectional study stratified by age (5–17yr), ethnicity (non-Hispanic white, non-Hispanic black, Hispanic, Asian, and Native Hawaiian or Pacific Islander (NHOPI)), sex, and BMI z-score. [15] Recruitment quotas were designed to represent a continuum of body types spanning underweight, healthy, and overweight ranges as determined by BMI z-score. BMI z-score cutoff boundaries were −2, −1, 0, 1, and 2. Tanner staging was self-reported by participants and not used as a stratification variable. Age in years was used as the surrogate variable. This cohort was deliberately designed to continuously span the most comprehensive range possible of body shapes and compositions of children aged 5–17. A diverse dataset with densely sampled examples across the spectrum of expected body compositions and ages enables the derivation of more accurate and body shape and composition models that generalize better to unseen data. The scope of inclusion of our study allows for our model to be compatible with any child who falls within the ranges of our dataset specified in Table 1.

Participants were screened for study eligibility via phone interview and excluded if they could not stand unassisted for two minutes or lie motionless for ten minutes, had metal implants, or had major body-shape-altering procedures (e.g., liposuction, amputations, etc.). No pregnant or lactating individuals were included in the study. Written informed consent was obtained from each participant upon arrival and all procedures were approved by

the Pennington Biomedical Research Center (PBRC; IRB study #2017–10, Federalwide Assurance #00006218); University of California, San Francisco (UCSF; IRB #16–20197); and University of Hawaii Office of Research Compliance (UH ORC; Center of Health Sciences #24282). The study is publicly listed on ClinicalTrials.gov as ID NCT03706612.

DXA Scans.—Reference total and compartmental body composition measurements were defined by DXA. We acquired single whole-body scans of each participant on either a Hologic Horizon/A system (UCSF) or a Discovery/A system (PBRC and UHCC) (Hologic Inc., Marlborough, MA, USA). Participants were positioned and scanned according to the respective manufacturer's guidelines. All scans were analyzed by a single certified technologist at UHCC using Hologic Apex version 5.6 with the National Health and Nutrition Examination Survey (NHANES) Body Composition Analysis calibration option disabled [17]. DXA systems quality control was performed by monitoring the weekly values of the Hologic Whole Body Phantom. Cross-calibration was checked between sites using a whole-body phantom scanned at each site, and calibrations were performed to compensate for systemic bias in all DXA measurements.

3D Optical Scans.—Inputs to our prediction model for training and testing were collected via 3D optical scanning. Scanners output unordered and unstructured point clouds representing the 3D surface geometry of the scanned participant. Participants wore form-fitting tights, a swim cap, and sports bra if female. Each participant was scanned in one or more 3DO systems pending availability at each recruiting location. We used three different 3DO system manufacturers across all sites: System 1 (Fit3D Proscanner 4.x, Fit3D Inc, Redwood City, CA, USA), System 2 (Styku S100 4.1, Styku LLC, Los Angeles, CA, USA), and System 3 (Size Stream SS20, Size Stream, Cary, NC, USA). Scans from different systems differed slightly in pose, although all were upright with straight elbows and knees in a neutral A-pose, and differed significantly in vertex count, spanning three orders of magnitude from 4,000 to 400,000 points. Scans were scaled to metric units and rotated and translated to align with System 1 orientation and positioning. This rigid transformation aligned the feet of all scans were aligned with the ZX plane as the ground plane and the origin as the center point midway between the arches, as shown in Figure 1. Height normalization was not performed on a per-subject basis as scanners were calibrated to agree on metric length scales. No pose normalization was performed on the scans. Minor discrepancies in scale or pose on an individually varying basis after these preprocessing steps were treated as data sampling noise consistent with future in-the-wild applications that our model was expected to learn to be agnostic towards. No other variables from the 3D scanner other than the raw 3D position information of the body surface were used in our model. Each participant was scanned on all three devices. This was done to train the shape and regression models to behave agnostically with respect to scanning machinery specific variations. Pose and scan quality varied slightly based on scanning technology. Sampling each participant on multiple scanners allows us to generate augmentation data on a limited cohort and train the model to account for scanner induced noise in the input data [16]. Participants were scanned twice on each system to gather a test-retest precision evaluation data set. As these scanning devices were often designed for adult dimensions and were not calibrated for the stature of small children, some scans were excluded from the study due to

scanning defects. Scans were excluded using quality control procedures looking for a priori quality issues including scan artifacts, excessive spatial noise, and incomplete scans [15]. No differences were noted in the study outcome variables between scans included and excluded due to participant demographics. An example of the differences present in different device captures of the same individual is shown in Figure 1.

There were 145 and 206 meshes in the training set for males and females, respectively. For Systems 1, 2, and 3, respectively, there were 57, 53, and 35 males scans and 88, 68, and 50 female scans in the training set. There were 52 and 80 meshes in the test set, with 26, 15, 11 males and 35, 25, 11 females for Systems 1, 2, and 3 respectively. Using a standardized significance level of 0.05, a desired power level of 0.8, and a standardized effect size of 0.2, 0.5, and 0.8 for small, medium, and large effect sizes respectively as suggested by Cohen's d, the number of observations required for a well-powered study are 394, 64, and 26. 0.56 is the minimum effect size our study is powered to detect in the male model given the smaller 52-member cohort while 0.45 is the minimum for females with 80 test scans. Our study is well-powered to detect a large effect size in males and a medium effect size in females.

Male and female models were trained and tested separately. All participants in the dataset were represented by between one and three scans. Data acquisition protocol specified two scans on each of three scanning devices in order to generate augmentation data and retest precision data. However, some scans were dropped from the dataset due to poor quality or incompleteness [15, 16]. Because participants were scanned with more than one scanning system, there were only 83 and 119 unique participants in the training set for males and females respectively, and 30 and 38 unique participants in the test set. The test set was a randomly selected set of 20% of the total unique participants.

3D Scan Templating and Shape Model Construction

In order to estimate the body composition of novel unorganized 3D scans, we constructed a unified PCA body shape model spanning the minor pose variance observed among our three scanning devices using an automatic templating procedure as specified in Tian et al. [16]. Our initial bootstrap sets consisted of 107, 28, and 25 fitted female meshes from System 1, 2, and 3, respectively, and 75, 12, and 9 fitted male meshes. The bootstrap set meshes were template-fitted with manually annotated landmarks as specified in Allen et al. [18] using a topologically consistent 60k mesh and combined into a single initial bootstrap PCA shape model.

The bootstrap PCA model was used to initialize an automated fitting procedure to produce a final unified autofit PCA model consisting of 60k autofits of all training scan meshes. We created a random 80/20 training/test set split sorted on participant IDs instead of individual mesh files, resulting in 39 female and 30 male IDs in the test set. Since we split training and test by participant ID and not by mesh ID, we ensured no participant had one system's scan in training while another separate mesh was in test. This resulted in a test set mesh count consisting of 80 female and 52 male raw scans as some participants were scanned in up to three different scanning systems. We deformed a 60k template by optimizing its principal component domain parameters in the bootstrap model to coarsely fit all raw training scans

from all devices, totaling 88, 68, and 50 female scans, and 57, 53, and 35 male scans from Systems 1, 2, and 3 respectively. This was done by optimizing the L2 regression objective:

$$E(\mathbf{w}) = \|\mathbf{A}\mathbf{w} - \mathbf{b}\|_2 + \|\mathbf{\Lambda}(\mathbf{w} - \mathbf{w}_0)\|_2 \quad (1)$$

where

$$\mathbf{b} = \mathbf{y} - \boldsymbol{\mu} \quad (2)$$

for PCA transformation matrix $\mathbf{A}$, PCA mean vector $\boldsymbol{\mu}$, regularization matrix $\mathbf{\Lambda}$, target surface $\mathbf{y}$, and initialization shape vector $\mathbf{w}_0$. We solve for w by performing iterative least squares optimization. At each step, we populate the target surface vector y with the closest points in the 3DO scan to the vertices of the current fitted surface estimate represented by $\mathbf{A}\mathbf{w} + \mathbf{b}$, and then solve for w via linear least squares. Since this method assumes rough anatomical alignment between the template and the target meshes, an initialization vector comprised of [height, weight, age] was used to seed the template mesh shape and start the vertex pairing from $\mathbf{w}_0$, the expected shape of an individual with those defined dimensions, instead of $\boldsymbol{\mu}$, the population mean. $\mathbf{\Lambda}$ was a diagonal matrix with $\frac{\sqrt{\lambda}}{\sigma_i}$ at each entry, where λ was a regularization strength hyperparameter (set to 0.001) and σ_i was the standard deviation of the ith PCA component. PCA parameters $\mathbf{w}$ were optimized and new pairings $\mathbf{y}$ were computed iteratively until norm of the difference between $\mathbf{w}^k$ and $\mathbf{w}^{k-1}$ was less than a convergence hyperparameter (0.1) for iteration k.

This coarse PCA deformation resulted in an intermediate mesh shape that was close to the target raw scan and was anatomically constrained by the standard deviations of each PCA basis parameter instead of manually assigned vertex targets. This allowed us to automate the fitting procedure and scale our method to much larger datasets. A surface-to-surface alignment from [18] was used to create a final refined fit that brought the coarse-fit 60k template into close alignment with the raw scan. This method was described in greater mathematical detail in [16] for adult participants.

We constructed a new unified autofit PCA space from the automatically templated training meshes consisting of 206 females and 145 males from all three scanning systems. This PCA model is the final model used for test set fitting and body composition prediction. We repeated the automated fitting procedure using the unified autofit PCA model as specified in [16] on the raw test set scans. A diagram of this multi-step process is shown in Figure 3.

Statistical Considerations.—In this study, our goal was to generate estimates of body composition from 3DO scans. We learned body composition metrics from the projected PCA coordinates of our final refined training mesh fits in a manner similar to [16]. For all templated 60k meshes in the training set, we found the projected PCA coordinate vector $\mathbf{w}$ by multiplying its flattened 3D coordinate vector $\mathbf{s}$ with the transpose of the PCA basis, $\mathbf{A}^{\mathrm{T}}$, which is also its inverse.

$$\mathbf{w} = \mathbf{A}^{\mathrm{T}}\mathbf{s} \tag{3}$$

We learned a regression matrix **M** that best maps the projected PCA basis coefficients of all training meshes **W** to the DXA body composition measurement vector of all training meshes **Y**.

$$\mathbf{Y} = \mathbf{MW} \tag{4}$$

Previous work learned the regression from shape PCA to body composition on the first *k* components that explained 95% of the shape variance in the training data [14] or all available PCA components using ordinary least squares (OLS). [16] In this work, we used a Least Angle Regression (LARS) [19] procedure to select the weights of our prediction model. We chose k=61 and k=40 for females and males respectively, as those were the number of components that explained 99.9% of the shape variance in the training set for each gender. Height, weight, age, and BMI were appended as additional regression features. We used this LARS model trained on the unified autofit training set to predict the body composition of the held-out test set scans after automatic template fitting and refined surface alignment. For comparison to LARS, we estimated body composition using four additional kinds of ensemble learning methods when mapping optimized PC coordinates to body composition: Decision tree [20], random forest [21], AdaBoost [22], and Gradient Boost [23].

We compared the predicted body composition values against DXA reference with the coefficient of determination (R^2), root-mean-squared error (RMSE), and Student's t-test.

A *p*-value of less than the Bonferroni corrected significance threshold of 0.004 for 12 measurements is undesirable as it indicates a significant difference between the means of DXA and our predictions from 3D templated scans.

To visualize the effect of changing scalar metrics on body shape, we solved the inverse regression problem that maps changes in a set of metrics of interest $\Delta\mathbf{Y}$ to a change in principal component coefficients $\Delta\mathbf{W}$ with matrix **X** analogous to section 4.3 of [18]:

$$\Delta\mathbf{W} = \mathbf{X}\Delta\mathbf{Y} \tag{5}$$

We apply the shape offset $\Delta\mathbf{W}$ to the scanned shape as discussed in [16] and [18] to simulate a change in a body composition variable, or for growing children, an advancement in age.

A web-GUI implementation of this method is available for public trial at https://shapeup.shepherdresearchlab.org/3do-bodycomp-analyzer/.

RESULTS

DXA reference values for the study population are shown in Table 1. Training and test set properties were not significantly different for any measured variable (*p*-value > 0.004 after Bonferonni correction). A visualization of the distribution of scans by device for each age

group in the training set is shown in Figure 2. Age categories were delimited based on recruitment stratification in Shape Up! Kids.

An example of an automated 60k templated fit from the test set fit using our method is shown in Figure 4.

Body composition prediction accuracy and *t*-tests against DXA from automated 3D optical scan fits for the LARS method are shown in Table 2. The values are mostly higher than the analogous results on adults in Tian et al. with the exception of male visceral fat. No predictions were significantly different from DXA measurements except for male trunk lean mass. The Demographics Only column shows the baseline regression accuracy using only the supplied initialization variables [height, weight, age] in the absence of any PCA shape information. Improvement upon these values justifies our methods for increasing the composition prediction accuracy beyond regressions from just the initialization scalars. All predicted metrics were better in our 3D template fit predictions than the baseline predicted by height, weight, and age with no shape fitting. Even in metrics that started at very high R^2 values such as lean mass and trunk lean, the RMSE values improved by as much as 20–40% after 3D fitting. A breakdown of prediction values by scanning device is shown in Table S1 of the Supplemental Data to detect biases in any single scanning system. Only visceral fat in both sexes was significantly different from DXA and underperformed relative to the combined cohort. No other biases were detected. None of the other ensemble learning methods (decision tree, random forest, AdaBoost, and Gradient Boost) performed as well as LARS method (data not shown). LARS regression was in practice only different from an OLS solution on the full component vector by around 0.02 R^2 on test data, but was a more conservative model as it used less than a third of the total variables to learn the mapping.

Table 3 shows test-retest precision of the 3DO estimates as measured by the coefficient of variation (%CV) and defined in Glüer et al. [24]. Duplicate DXA scans were not acquired to be radiation dose conserving. Shepherd *et al.* [25] showed that the %CV of DXA in children aged 6–16 on bone mineral density and content was age dependent but typically less than 2%. Although we lose some precision with our optical method, we note that we gain the ability to collect multiple data points in rapid succession or over a longitudinal study without risk of radiation exposure.

We computed the delta-weight vector corresponding to age changes, and added this vector to a templated scan multiplied by a constant to represent change in years as in section 4.3 of [18]. This process can generalize to any number of variables, but in our visualization, we solved for a hyperplane over the age / BMI domain and kept BMI fixed while incrementing age in order to visualize the effect of aging for an individual of those particular dimensions. Figure 5 shows examples of extrapolating young children to 18 years of age while keeping predicted BMI constant. A high and a low BMI example was tested for a male and a female participant.

These extrapolated images capture the effects of puberty in its age-progression deformation, such as changes in limb proportions and development of secondary sex characteristics. Since Tanner staging was self-reported and thus not used as a stratification variable in this study,

age served as the prior for pubertal maturity in our model. Figure 6 shows expected body shapes generated using our PCA model for a female measuring 1.6m tall and 50kg at ages 9, 13, and 17. This regularization allowed our model to disentangle pubertal maturity from individuals of similar stature, a distinction that was not necessary in prior work on adult cohorts.

Figure 7 shows Bland-Altman plots with associated best-fit lines for fat mass, lean mass, and visceral fat for female and male test set predictions respectively. Equations for the best-fit lines on each plot and the *p*-values for the coefficients are shown in the top right corners. This study was designed to develop a model that could perform generalized device, age, and shape agnostic body shape and composition predictions to any 3DO input that fell within the bounds of our training parameters and not to distinguish differences between scanners or groups. Prediction models learned continuous interpolations of densely sampled body shape variation within a representative population and thus required inclusion of a diverse range of training and testing examples in the experimental cohort. The plots on Figure 7 show that outliers are uniformly distributed. Our method achieves consistently accurate predictions across the range of body compositions in our test data without significant bias.

DISCUSSION

We presented the most complete 3DO-based solution for total and regional body composition analysis in children and adolescents at the time of writing. Wells et al. [26] studied a sample of 1484 children between the ages of 5–11 with 3DO scanning but only tested the accuracy of collecting scalar anthropometric features from scans without consideration of body composition. Santos et al. [27] used the features collected by this method to construct a PCA space similar to our work, but only analyzed the correlation between individual principal components with anthropometric and body composition measurements and did not actually predict the body composition metrics of test data. Our method takes raw, unformatted 3DO scans as input and predicts 12 body composition variables end-to-end with no intermediate manual processing required. Our automated system enabled fast processing of raw 3DO scans that yielded 3–5 times more templated meshes for some scanning systems than were previously available through the manual annotation pipeline. Our method worked on young children and adolescents despite the greater range of body size variation among this age group relative to an adult-only cohort.

Our study is currently underpowered for small effect sizes in females and medium effect sizes in males. With a target recruitment of 720 total individuals for Shape Up! Kids (NCT03706612) and an approximate 50/50 sex distribution, our study is not powered to detect a small effect size of d=0.2 between DXA and 3DO prediction. The power level of our study will not affect the primary metric of accuracy used for determining agreement between two measurements, R^2 and RMSE, or the precision of repeat trials (%CV). A study underpowered for small effect sizes may prevent us from detecting a statistically significant, systemic bias between 3DO prediction and DXA as measured by the *p*-value in Table 2.

The wide variation of body shapes between young children and more mature teens presents additional challenges for evaluating body composition in a pediatric population.

For example, although a BMI of 17 in Figure 5B is not alarming, an associated 37% body fat increases cardiovascular disease risk by 2–4 times in adults [28]. Our model predicted this value to fall to 33% at age 18. Intervention could be recommended based on current body fat percentage but not current BMI. Additional work is required to accurately model how individual bodies change shape and composition over time as influenced by puberty and maturity.

We tried four kinds of ensemble learning methods when mapping optimized PC coordinates to body composition: Decision tree, random forest, AdaBoost, and Gradient Boost. We found that these alternatives to LARS did not perform as well with this data type. None of them were close to achieving an 0.85 R^2 for fat mass on the test data. Such methods may be more useful when larger datasets are available, as fragmenting an age 5–17 cohort into many subsets creates heavily biased, weak estimators that do not perform well on test data that may be drastically different from the training data.

We tried alternatives to PCA for constructing a body shape latent space, namely supervised dimensionality reduction using linear discriminant analysis (LDA) [29] with percent fat and visceral fat mass as discriminant variables, and nonparameterized prediction methods such as Gaussian Process Regression (GPR) [30]. PCA had advantages over both methods. LDA created projections that cluster data points around their assigned labels, which did not translate well to continuous regression. GPR performed better than parameterized regressions in our previous adult study [16] but the test dataset was too small to adequately compare PCA to GPR.

Children have a lower safety tolerance for X-ray radiation than adults [29], and this imposes a single scan limit with a long minimum time interval between scans. Although the precision of our 3DO method for body composition estimation is 2–5 times lower that of DXA bone density precision on kids, this limitation can be mitigated due to the ease of repeating of 3DO scanning. As we showed in Tian et al. [16], the least significant change (LSC) [32] is:

$$LSC = 2.77 * RMSE_{precision}$$

This value drops with the square root of the sample number [33]. The LSC for fat mass is around 2kg for children. Four samples at a given time point is enough to drop the LSC below 1kg, which is comparable to the LSC of DXA on adults from Tian et al [16]. As each scan takes around a minute, is radiation-free, and can be processed automatically, this increase in procedure time is an acceptable trade off to improving the monitoring precision. The speed of the scan capture is especially valuable for very young children, as they have greater difficulty staying still for the requisite amount of time needed for DXA or MRI (10–30 minutes).

2 scans on each of 3 scanning systems were collected as part of the data protocol to train our model to be robust and agnostic to pose variation and scanner specific geometry characteristics. However, some scans were dropped due to hardware or software errors on the side of the scanner manufacturer. Future data captures may opt to collect 3 or 4 scans on each system with the intent of both lowering the LSC and to build in redundancy in the

data capture such that a minimum floor of 6 scans, two on each device, can be guaranteed for every participant in the dataset.

Pose variation is more extreme in younger children than in adults or postpubescent teens. Fixed handrail and feet placements in some scanners will naturally cause more arm and leg abduction for smaller bodies and could introduce additional variations in the shape model that do not correlate well to body compositions. We experimented with a regression from all 60k vertices in the test set to body composition instead of from PCA coefficients, eliminating compression loss from the PCA encoding as a source of error. These results were similar (within 0.02 R2 in either direction) to PCA coefficient regression, suggesting the variance in the shapes themselves contribute to most of the inaccuracy. Pose normalization [34] may focus the variance of the 3D shapes on physiological change and decrease the impact of pose on the shape model, leading to more precise predictions of body composition.

This study has several limitations left to be addressed by future work. Shape differences between individuals of different ages are much more drastic in a 5–17 aged cohort than in an adult study and can vary substantially between individuals of the same age depending on rate of growth and maturity. It is necessary to have more data relative to an adult study to fully capture the continuum of growth and variation in the preteen to teen age range. The currently available participant cohort is about half the size of the adult study population in. Additional data availability may increase the accuracy of the predictions by fully representing the variance between age ranges and scanners, enabling the use of more flexible nonlinear models such as GPR. Furthermore, because the bodies of juveniles and adolescents can change dramatically in a period of time that may be shorter than a typical clinical follow-up, longitudinal studies in this age range are required to isolate the relationship between body composition and body shape controlled for natural growth and maturation.

CONCLUSION

3DO imaging technologies can estimate body composition in children and adolescents with accuracy well correlated to and not significantly different from reference DXA measurements and provides estimates on many variables not accounted for by commonly used body composition measurement proxies, such as BMI. Precision error of our 3DO method is within 2–5 times that of DXA, a tradeoff that can be compensated for with repeat measurements. We applied a method for automatically fitting a topologically consistent 60k template mesh to arbitrary 3DO scans and predicting body composition metrics from the standardized meshes. Our previous work using this technique was only trained and tested on an adult population (age 18+) and was not assumed a priori to work on children and adolescents. Although the precision error as measured by %CV was worse than DXA bone mineral density benchmarks, the rapid (<1 minute) scan time and the lack of ionizing radiation allows for multiple samples to be collected either in quick succession to mitigate prediction noise or over a monitoring period to plot longitudinal change. Future work can focus on further reducing the barrier to collecting body composition data by allowing for predictions on 2D image inputs such as in [35].

Our method is safe and fast, with end-to-end automation between 3DO inputs and predicted outputs and can be deployed in non-clinical settings where radiological imaging would be prohibitively expensive. 3DO imaging is a promising tool for monitoring childhood obesity during a crucial developmental period that may have long-term implications on future health and metabolic risk.

Supplementary Material

Refer to Web version on PubMed Central for supplementary material.

Funding Disclosure:

AKG: NICHD #R01HD082166, National Institutes of Health NORC Center Grants (P30DK072476, Pennington/Louisiana and P30DK040561, Harvard); JAS: National Institute of Diabetes and Digestive and Kidney Diseases (NIDDK) (R01DK109008 and R01DK111698).

Conflict of Interest Statement:

JAS is a scientific advisor for Styku LLC and owns stock options. BC is employed by Google LLC and owns stock options. SBH is on the medical advisory boards of Tanita Corp. and Medifast Corp. and is a former employee of Merck & Co. SBH is an Amazon Scholar and owns stock options. Styku LLC and Fit3D Inc. contributed scanning equipment in support of NIH studies.

Abbreviations:

3DO	3-Dimensional Optical
60k	60,001 vertex mesh template
BMI	body mass index
DXA	dual X-ray absorptiometry
PCA	principal component analysis

References

1. Simmonds M, Llewellyn A, Owen CG, Woolacott N. Predicting adult obesity from childhood obesity: A systematic review and meta-analysis. Obesity Reviews. 2015;17(2):95–107. doi:10.1111/obr.12334 [PubMed: 26696565]
2. Sims E, Danforth E Jr, Horton ES, Bray GA, Glennon J, Salans L. Endocrine and metabolic effects of experimental obesity in man. Recent progress in hormone research. 1973;29:457. [PubMed: 4750591]
3. Freidenberg G, Reichart D, Olefsky J, Henry R. Reversibility of defective adipocyte insulin receptor kinase activity in non-insulin-dependent diabetes mellitus. Effect of weight loss. Journal of Clinical Investigation. 1988;82(4):1398. [PubMed: 3170749]
4. Schneider V, Oganov V, LeBlanc A, Rakhmanov A, Bakulin A, Grigoriev A, Varonin L. Space Flight Bone Loss and Change In Fat and Lean Body Mass. Journal of Bone and Mineral Research. 1992;7(Supp. 1).
5. Qatanani M, Lazar MA. Mechanisms of obesity-associated insulin resistance: many choices on the menu. Genes & development. 2007;21(12):1443–55. [PubMed: 17575046]
6. Price GM, Uauy R, Breeze E, Bulpitt CJ, Fletcher AE. Weight, shape, and mortality risk in older persons: elevated waist-hip ratio, not high body mass index, is associated with a greater risk of death. Am J Clin Nutr. 2006;84(2):449–60. Epub 2006/08/10. [PubMed: 16895897]

7. Simoni P, Guglielmi R, Gómez MP. Imaging of body composition in children. Quantitative Imaging in Medicine and Surgery. 2020;10(8):1661–1671. doi:10.21037/qims.2020.04.06 [PubMed: 32742959]
8. Cahoon GD, Davison TE. Prediction of compliance with MRI procedures among children of ages 3 years to 12 years. Pediatric Radiology 2014;44:1302–9. doi:10.1007/s00247-014-2996-y. [PubMed: 24859264]
9. Weber DR, Leonard MB, Zemel BS. Body Composition Analysis in the Pediatric Population. Pediatr Endocrinol Rev. 2012;10(1):130–139. [PubMed: 23469390]
10. Achamrah N, Colange G, Delay J, et al. Comparison of body composition assessment by DXA and BIA according to the body mass index: A retrospective study on 3655 measures. PLOS ONE. 2018;13(7). doi:10.1371/journal.pone.0200465
11. Ward LC. Bioelectrical impedance analysis for Body Composition Assessment: Reflections on accuracy, Clinical Utility, and standardisation. European Journal of Clinical Nutrition. 2018;73(2):194–199. doi:10.1038/s41430-018-0335-3 [PubMed: 30297760]
12. Tinsley GM, Moore ML, Benavides ML, Dellinger JR, Adamson BT. 3-dimensional optical scanning for body composition assessment: A 4-component model comparison of four commercially available scanners. Clinical Nutrition. 2020;39(10):3160–3167. doi:10.1016/j.clnu.2020.02.008 [PubMed: 32113641]
13. Ng BK, Hinton BJ, Fan B, Kanaya AM, Shepherd JA. Clinical anthropometrics and body composition from 3D whole-body surface scans. European Journal of Clinical Nutrition. 2016;70(11):1265–1270. doi:10.1038/ejcn.2016.109 [PubMed: 27329614]
14. Ng BK, Sommer MJ, Wong MC, et al. Detailed 3-dimensional body shape features predict body composition, blood metabolites, and functional strength: The shape up! studies. The American Journal of Clinical Nutrition. 2019;110(6):1316–1326. doi:10.1093/ajcn/nqz218 [PubMed: 31553429]
15. Wong MC, Ng BK, Kennedy SF, et al. Children and adolescents' anthropometrics body composition from 3-D optical surface scans. Obesity. 2019;27(11):1738–1749. doi:10.1002/oby.22637 [PubMed: 31689009]
16. Tian IY, Wong MC, Kennedy S, Kelly NN, Liu YE, Garber AK, Heymsfield SB, Curless B, Shepherd JA. A Device-agnostic shape model for automated body composition estimates from 3D optical scans. Medical Physics 2022; 1–15. 10.1002/mp.15843
17. Ng BK, Liu YE, Wang W, Kelly TL, Wilson KE, Schoeller DA, et al. Validation of rapid 4-component body composition assessment with the use of dual-energy X-ray absorptiometry and bioelectrical impedance analysis. The American Journal of Clinical Nutrition 2018;108:708–15. doi:10.1093/ajcn/nqy158. [PubMed: 30099474]
18. Allen B, Curless B, Popović Z. The space of human body shapes. ACM SIGGRAPH 2003 Papers on - SIGGRAPH '03. 2003. doi:10.1145/1201775.882311
19. Efron B, Hastie T, Johnstone I, Tibshirani R. Least angle regression. The Annals of Statistics. 2004;32(2). doi:10.1214/009053604000000067
20. Myles AJ, Feudale RN, Liu Y, Woody NA, Brown SD. (2004). An introduction to decision tree modeling. Journal of Chemometrics: A Journal of the Chemometrics Society, 18(6), 275–285.
21. Qi Y (2012). Random forest for bioinformatics. In Ensemble machine learning (pp. 307–323). Springer, Boston, MA.
22. Freund Y and Schapire RE. A decision-theoretic generalization of on-line learning and an application to boosting, J. Comput. Syst. Sci, 55(1):119–139, 1997
23. Sun R, Wang G, Zhang W, Hsu LT, & Ochieng WY. (2020). A gradient boosting decision tree based GPS signal reception classification algorithm. Applied Soft Computing, 86, 105942.
24. Glüer C-C, Blake G, Lu Y, Blunt BA, Jergas M, Genant HK. Accurate assessment of precision errors: how to measure the reproducibility of bone densitometry techniques. Osteoporosis Int. 1995;5(4):262–270.
25. Shepherd JA, Wang L, Fan B, et al. Optimal monitoring time interval between DXA measures in children. Journal of Bone and Mineral Research. 2011;26(11):2745–2752. doi:10.1002/jbmr.473 [PubMed: 21773995]

26. Wells JC, Stocks J, Bonner R, et al. Acceptability, precision and accuracy of 3D photonic scanning for measurement of body shape in a multi-ethnic sample of children aged 5–11 years: The Slic Study. PLOS ONE. 2015;10(4). doi:10.1371/journal.pone.0124193
27. Santos LP, Ong KK, Day F, et al. Body shape and size in 6-year old children: Assessment by three-dimensional photonic scanning. International Journal of Obesity. 2016;40(6):1012–1017. doi:10.1038/ijo.2016.30 [PubMed: 26880232]
28. Macek P, Biskup M, Terek-Derszniak M, et al. optimal body fat percentage cut-off values in predicting the obesity-related cardiovascular risk factors: A cross-sectional cohort study. Diabetes, Metabolic Syndrome and Obesity: Targets and Therapy. 2020;Volume 13:1587–1597. doi:10.2147/dmso.s248444 [PubMed: 32494175]
29. Xanthopoulos P, Pardalos PM, & Trafalis TB (2013). Linear discriminant analysis. In Robust data mining (pp. 27–33). Springer, New York, NY.
30. Schulz E, Speekenbrink M, & Krause A (2018). A tutorial on Gaussian process regression: Modelling, exploring, and exploiting functions. Journal of Mathematical Psychology, 85, 1–16.
31. Minigh J (2005). Pediatric radiation protection. Radiologic technology, 76(5), 365–379. [PubMed: 15921016]
32. Shepherd JA, Lu Y. A generalized least significant change for individuals measured on different DXA Systems. Journal of Clinical Densitometry. 2007;10(3):249–258. doi:10.1016/j.jocd.2007.05.002 [PubMed: 17616413]
33. Bonnick SL. Monitoring changes in bone density. Women's Health. 2008;4(1):89–97. doi:10.2217/17455057.4.1.89
34. Wong MC, Ng BK, Tian I, et al. A pose-independent method for accurate and precise body composition from 3D optical scans. Obesity. 2021;29(11):1835–1847. doi:10.1002/oby.23256 [PubMed: 34549543]
35. Tian IY, Ng BK, Wong MC, et al. Predicting 3D body shape and body composition from conventional 2D photography. Medical Physics. 2020;47(12):6232–6245. doi:10.1002/mp.14492 [PubMed: 32978970]

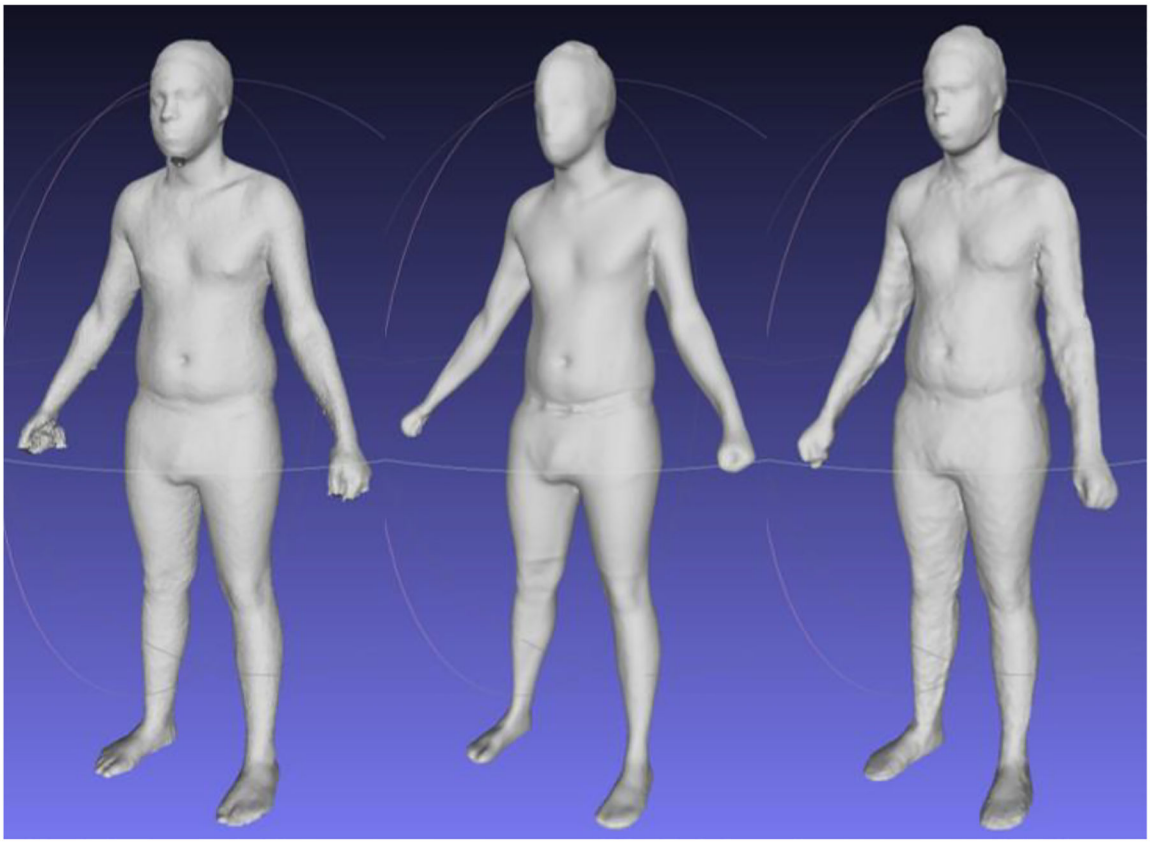

Figure 1.
Scans of a 14-year-old male on Systems 1, 2, and 3 respectively.

Figure 2.
Scan count for each scanning device in each age category.

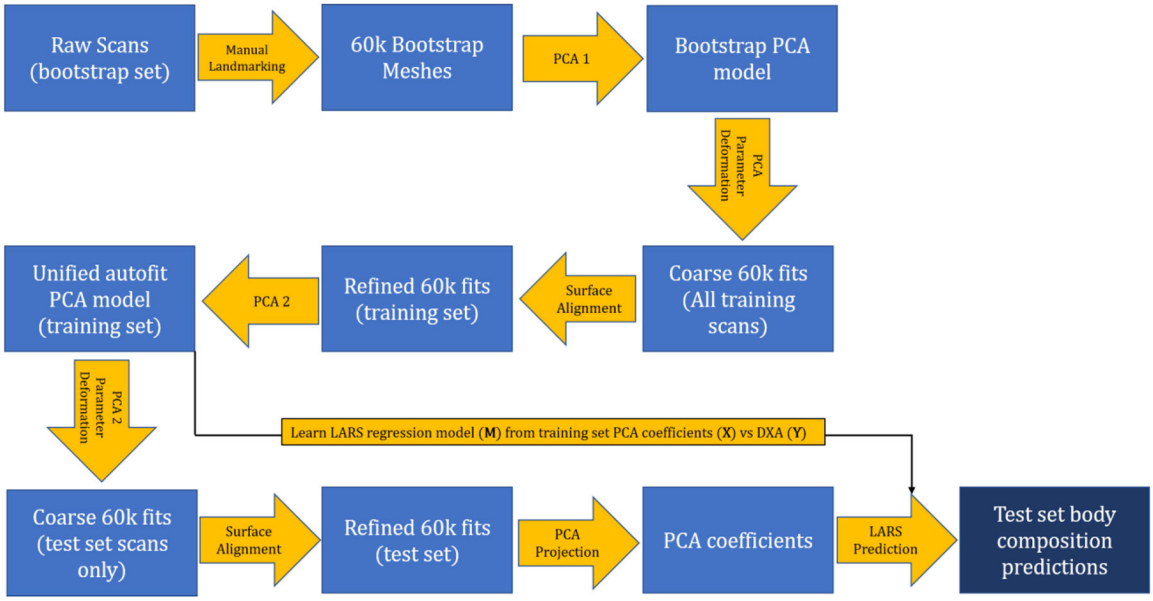

Figure 3.

Diagram showing workflow to produce body composition predictions for unseen test scans. Operations in each row corresponds to bootstrap, training, and test data respectively.

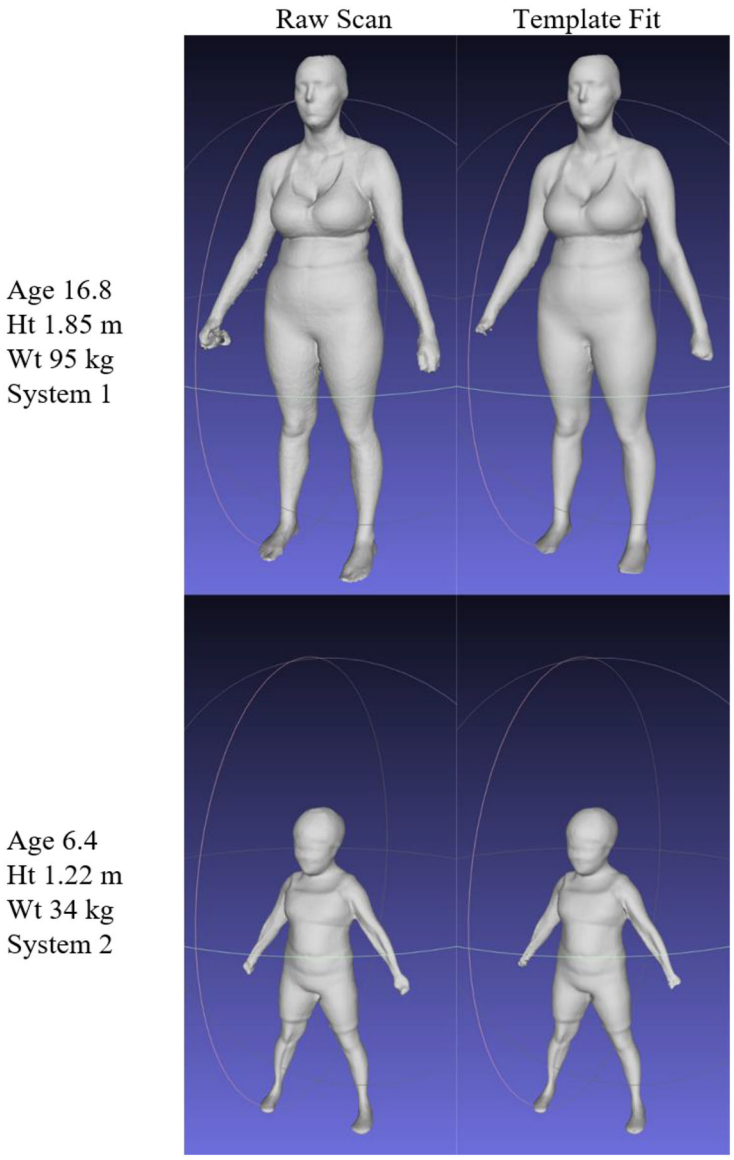

Figure 4.

Automated template fitting results on two females from the test set at opposite ends of the physical maturity spectrum. Top subject was a very tall 16-year-old and had adult like proportions, scanned on System 1 with 404k vertices in the raw file. Bottom subject was a very small 6-year-old scanned on System 2 with 51k vertices.

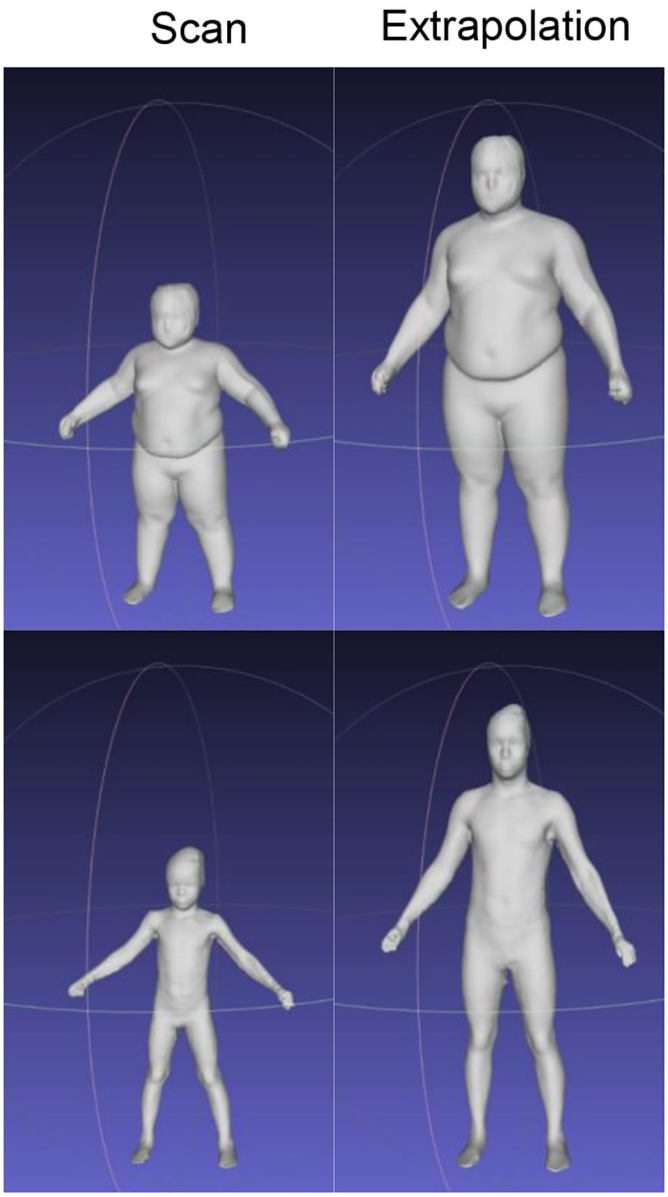

(A)

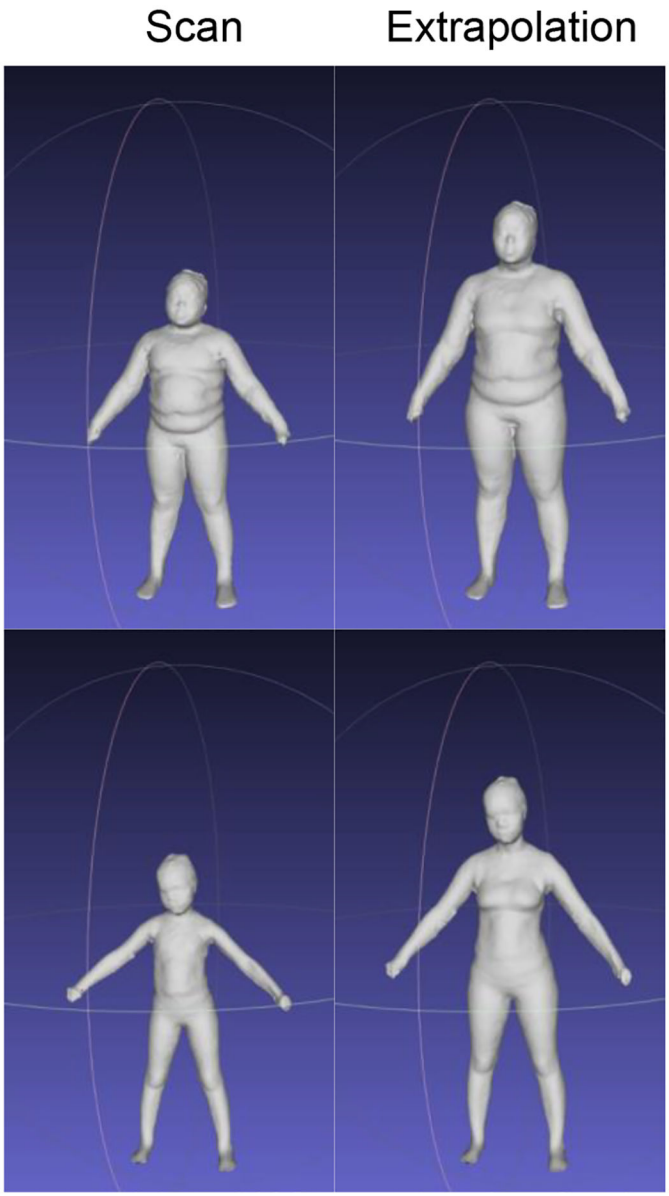

Figure 5.

(A) Two males scanned at 7 (top) and 8 (bottom) years of age with BMIs of 40 and 16, extrapolated to age 18. Starting DXA measured percent fats were 50% and 21% respectively. Extrapolated percent fats were 35% and 18%. (B) Two females scanned at 9 (top) and 7 (bottom) years of age with BMIs of 29 and 17, extrapolated to age 18. Starting DXA measured percent fats were 47% and 37%. Extrapolated percent fats were 39% and 33% respectively.

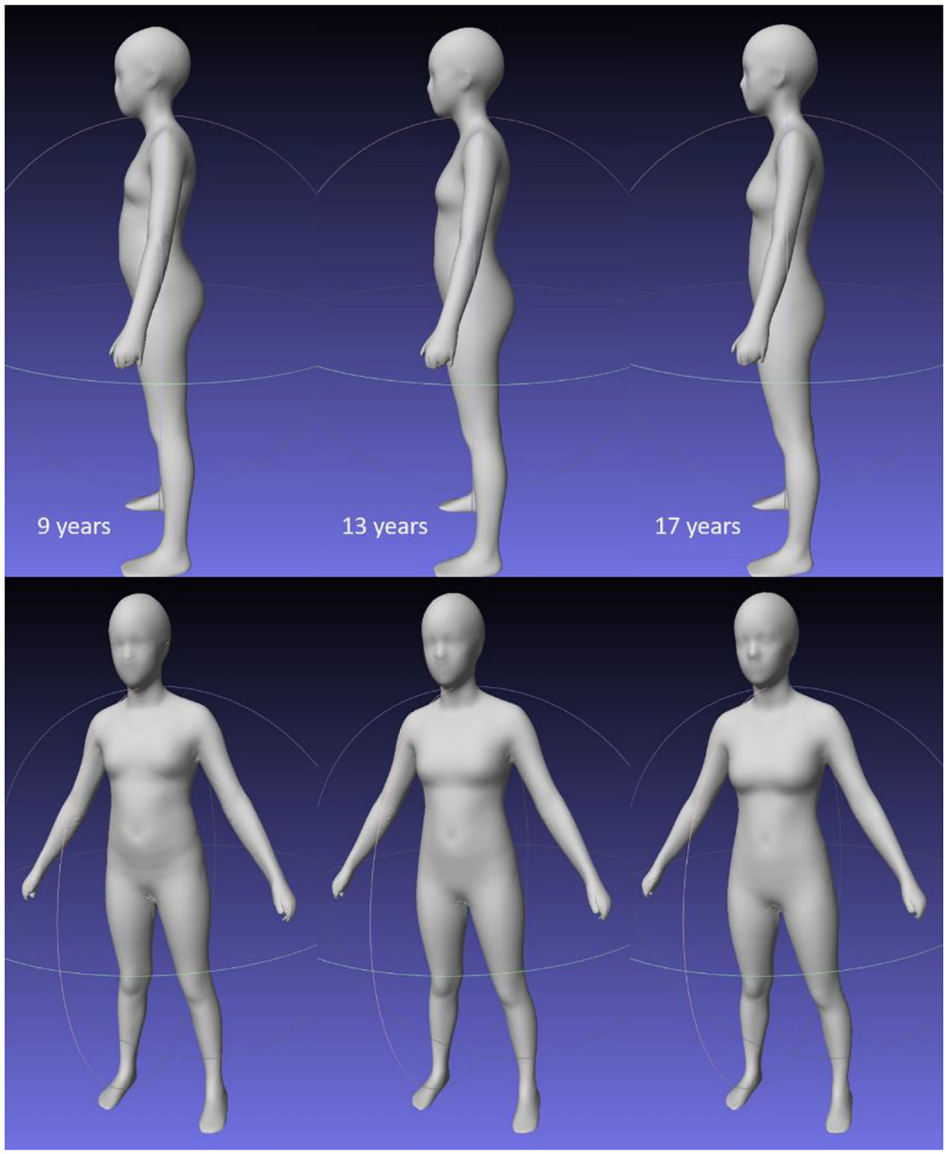

Figure 6.

Generated average shapes for a 1.6m, 50kg female at ages 9, 13, and 17. Tanner staging was self-reported and not used in this study; we use age as a surrogate in this study to act as the prior for pubertal development in our model.

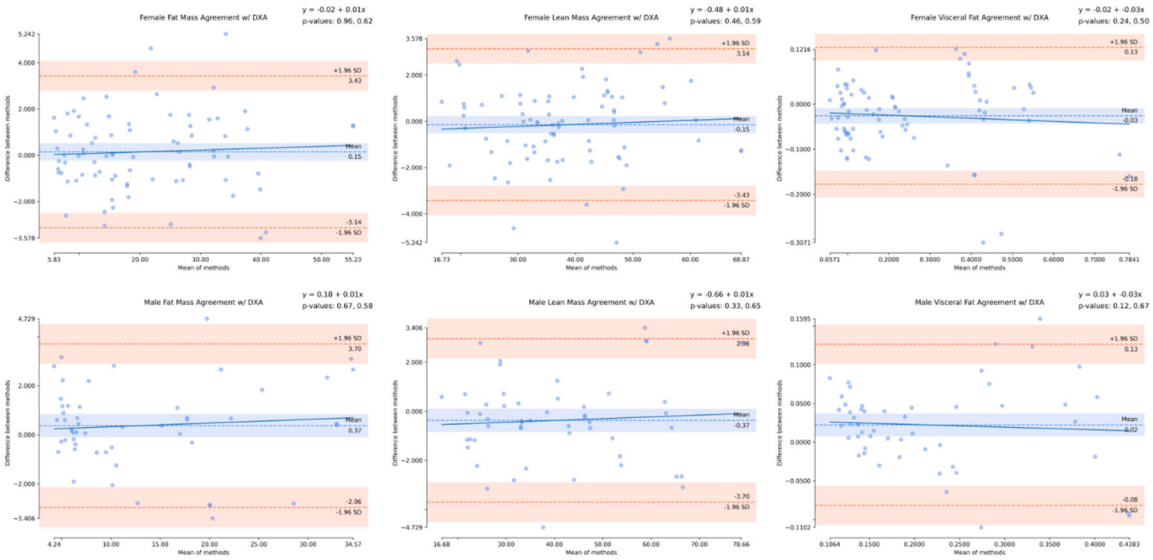

Figure 7.

Bland-Altman plots for fat mass, lean mass, and visceral fat for female and male test set predictions with best-fit line equations. Best fit line equation and p-value for the coefficients are shown in the top right corners. No significant biases were detected.

Table 1.

DXA reference measurement statistics for unique individuals in the training and test sets. Plus-minus values are standard deviation. p-values represent significance values for the t-test between the means of training and test sets.

	Male						
	Train (N = 83)			**Test (N = 30)**			***p*-value**
	Mean ± SD	**Min**	**Max**	**Mean ± SD**	**Min**	**Max**	
Age (Years)	11.7 ± 3.0	5	17	11.8 ± 2.8	7	17	0.9
Height (m)	1.5 ± 0.2	1.1	1.9	1.5 ± 0.2	1.3	1.8	1.0
Mass (kg)	55.2 ± 24.5	20.7	145.6	53.3 ± 21.5	23.0	107.2	0.7
BMI	22.1 ± 6.6	14.4	53.0	21.8 ± 5.8	14.6	39.5	0.8
BMI-z	0.8 ± 1.2	−2.3	3.2	0.7 ± 1.2	−2.1	3.0	0.8
% Fat	24.1 ± 9.6	8.5	46.7	23.7 ± 9.2	9.0	50.1	0.8
Lean Mass (kg)	41.2 ± 16.3	16.7	86.9	40.2 ± 15.7	17.0	80.1	0.8
Fat Mass (kg)	14.0 ± 11.2	3.9	68.0	13.1 ± 8.7	4.3	35.9	0.7
Visceral Fat (kg)	0.2 ± 0.1	0.02	0.9	0.2 ± 0.1	0.1	0.4	1.0
Leg Lean (kg)	7.0 ± 3.0	2.4	15.8	6.8 ± 2.9	2.4	14.1	0.8
Arm Lean (kg)	2.3 ± 1.1	0.8	5.6	2.3 ± 1.1	0.8	5.0	1.0
Trunk Lean (kg)	19.1 ± 7.7	7.3	39.7	18.3 ± 7.5	7.7	37.4	0.6
Trunk Fat (kg)	5.4 ± 5.5	1.0	34.9	4.9 ± 3.9	1.2	14.7	0.6
Leg Fat (kg)	3.0 ± 2.1	0.8	11.9	2.9 ± 1.8	1.0	8.0	0.8
Arm Fat (kg)	0.9 ± 0.8	0.2	4.1	0.8 ± 0.8	0.2	2.4	0.6
FMI	5.8 ± 3.9	1.6	21.9	5.5 ± 3.7	2.0	19.7	0.8
FFMI	16.6 ± 4.1	11.6	36.8	16.2 ± 3.1	10.8	24.1	0.6

	Female						
	Train (N = 119)			**Test (N = 38)**			***p*-value**
	Mean ± SD	**Min**	**Max**	**Mean ± SD**	**Min**	**Max**	
Age (Years)	12.2 ± 3.2	5	17	12.9 ± 3.2	6	17	0.2
Height (m)	1.5 ± 0.1	1.1	1.8	1.5 ± 0.1	1.2	1.9	0.5
Mass (kg)	53.5 ± 20.8	18.4	140.4	59.6 ± 22.0	27.1	124.1	0.1
BMI	22.7 ± 6.4	13.1	52.2	25.0 ± 7.3	14.1	46.9	0.1
BMI-z	0.8 ± 1.2	−2.4	2.9	1.0 ± 1.2	−1.5	2.6	0.3
% Fat	31.2 ± 7.3	13.9	47.9	33.1 ± 8.0	17.7	47.2	0.2
Lean Mass (kg)	35.8 ± 11.0	13.3	74.4	38.8 ± 11.7	17.2	68.2	0.2
Fat Mass (kg)	17.7 ± 10.8	4.0	66.0	20.8 ± 11.4	6.2	55.9	0.1
Visceral Fat (kg)	0.2 ± 0.2	0.01	0.8	0.2 ± 0.2	0.03	0.7	0.5
Leg Lean (kg)	6.0 ± 2.1	1.7	12.3	6.5 ± 2.1	2.4	11.2	0.2
Arm Lean (kg)	1.9 ± 0.6	0.7	4.1	2.0 ± 0.7	0.9	3.9	0.1
Trunk Lean (kg)	16.9 ± 5.5	6.2	37.5	18.4 ± 5.8	8.0	34.3	0.2

	Female						
	Train (N = 119)			Test (N = 38)			*p*-value
	Mean ± SD	Min	Max	Mean ± SD	Min	Max	
Trunk Fat (kg)	7.2 ± 5.4	1.1	33.4	8.9 ± 6.2	1.8	31.5	0.1
Leg Fat (kg)	3.7 ± 2.0	0.9	11.0	4.2 ± 1.9	1.5	7.9	0.2
Arm Fat (kg)	1.1 ± 0.8	0.2	4.8	1.3 ± 0.8	0.3	4.0	0.1
FMI	7.4 ± 3.8	2.2	24.4	8.7 ± 4.3	2.8	21	0.1
FFMI	15.2 ± 2.9	10.1	27.5	16.2 ± 3.3	10.7	25.7	0.1

Table 2:

Body composition prediction accuracy against DXA reference measurements on test data for 3D automated template fits. Shapes were fit using the full PCA basis (145 components for males, 206 components for females) but body composition was predicted on k components selected using LARS, where k = 40 for males and 61 for females. % fat was calculated as fat mass divided by known weight. p-values indicate difference from DXA measurement, where the Bonferroni corrected threshold for significance for 12 measurements is <0.004.

	Male, d=145, n=52			Female, d=206, n=80		
	R^2 (RMSE)	***p*-value (comparison of means)**	**Demographics Only R^2 (RMSE)**	**R^2 (RMSE)**	***p*-value (comparison of means)**	**Demographics Only R^2 (RMSE)**
% fat	**0.88** (3.55)	0.09	**0.70** (5.14)	**0.85** (3.20)	0.52	**0.68 (4.47)**
Lean Mass (kg)	**0.99** (1.74)	0.12	**0.96** (3.30)	**0.98** (1.68)	0.44	**0.97** (2.17)
Fat Mass (kg)	**0.96** (1.74)	0.12	**0.86** (3.30)	**0.98** (1.68)	0.44	**0.97** (2.17)
Visc. Fat (kg)	**0.65** (0.06)	0.004	**0.45** (0.07)	**0.78** (0.08)	0.004	**0.64** (0.1)
Leg Lean (kg)	**0.98** (0.4)	0.81	**0.96** (0.61)	**0.96** (0.45)	0.23	**0.92** (0.6)
Arm Lean (kg)	**0.96** (0.21)	0.81	**0.87** (0.39)	**0.90** (0.21)	0.020	**0.88** (0.24)
Trunk Lean (kg)	**0.98** (0.93)	0.002	**0.96** (1.52)	**0.98** (0.92)	0.14	**0.96** (1.14)
Trunk Fat (kg)	**0.91** (1.22)	0.93	**0.81** (1.78)	**0.96** (1.24)	0.24	**0.93** (1.64)
Leg Fat (kg)	**0.95** (0.43)	0.71	**0.83** (0.76)	**0.93** (0.5)	0.008	**0.89** (0.64)
Arm Fat (kg)	**0.93** (0.16)	0.07	**0.87** (0.22)	**0.95** (0.19)	0.22	**0.91** (0.25)
FMI	**0.97** (0.74)	0.08	**0.90** (1.19)	**0.97** (0.76)	0.41	**0.96** (0.9)
FFMI	**0.94** (0.74)	0.08	**0.86** (1.19)	**0.95** (0.76)	0.41	**0.93** (0.9)

Table 3.

Test retest precision for 3D auto templated composition predictions. All components were used for shape fitting. k components were selected using LARS for prediction regression, where k = 40 and 61 for males and females respectively.

	This Work			
	Male n=43		Female n=65	
	%CV	RMSE	%CV	RMSE
% fat	-	1.88	-	1.77
Lean Mass (kg)	1.84	0.75	2.23	0.88
Fat Mass (kg)	6.09	0.75	4.01	0.88
Visc. Fat (kg)	10.1	0.02	10.75	0.03
Leg Lean (kg)	2.53	0.17	2.06	0.14
Arm Lean (kg)	3.52	0.08	4.67	0.09
Trunk Lean (kg)	1.77	0.34	1.96	0.37
Trunk Fat (kg)	10.14	0.47	4.44	0.42
Leg Fat (kg)	6.79	0.19	5.07	0.23
Arm Fat (kg)	8.71	0.06	3.19	0.04
FMI	6.99	0.35	4.28	0.39
FFMI	2.18	0.35	2.37	0.39